Microstructure characteristics and corrosion behavior of metal inert gas welded dissimilar joints of 6005A modified by Sc and 5083 alloys

Guo-fu XU[1,2], Liang LIU[1], Ying DENG [1,2], Yu ZENG[3], Jun-chang CAO[1],
Lei TANG[1], Xiao-yan PENG[1], Jia-qi DUAN[4], Mei-chan LIANG[5], Qing-lin PAN[1]

1. School of Materials Science and Engineering, Central South University, Changsha 410083, China;
2. State Key Laboratory of Power Metallurgy, Central South University, Changsha 410083, China;
3. Baoshan Iron & Steel Co., Ltd., Shanghai 201900, China;
4. Warwick Manufacturing Group, The University of Warwick, Coventry, CV4 7AL, UK;
5. Guangdong Weiye Aluminum Factory Group Co., Ltd., Foshan 528000, China

Abstract: The corrosion behavior and microstructure characteristics of metal inert gas (MIG) welded dissimilar joints of the 6005A alloy modified with Sc (designated as 6005A+Sc) and the 5083 alloy were investigated using corrosion tests and microscopy techniques. Results show that the dissimilar joints exhibit strong stress corrosion cracking (SCC) resistance, maintaining substantial strength during slow strain rate tensile tests. Notably, the heat-affected zone (HAZ) and base metal (BM) on the 6005A+Sc side show superior performance in terms of inter-granular corrosion (IGC) and exfoliation corrosion (EXCO) compared to the corresponding zones on the 5083 side. The lower corrosion resistance of the 5083-BM and the 5083-HAZ can be attributed to the presence of numerous Al_2Mg_3 phases and micro-scaled $Al_6(Mn,Fe)$ intermetallics, mainly distributed along the rolling direction. Conversely, the enhanced corrosion resistance of the 6005A+Sc-BM and the 6005A+Sc-HAZ can be attributed to the discontinuously distributed grain boundary precipitates (β-Mg_2Si), the smaller grain size, and the reduced corrosive current density.
Key words: metal inert gas welding; dissimilar joint; aluminum alloy; corrosion, microstructure

1 Introduction

Due to the excellent post-weld mechanical properties, adaptability to various welding positions and the environmental friendliness, metal inert gas (MIG) welding technique is widely used in joining aluminum (Al) alloy components in transport, ships, and other structural industries [1−3]. During MIG process, it is inevitable to generate the gradient heat perpendicular to the welding direction. Therefore, three distinct zones, namely the fusion zone (FZ) with the highest temperature, the heat affected zone (HAZ), influenced by welding heat, and the base metal (BM), beyond HAZ maintaining its original state, are formed in the joints [4]. This thermal effect leads to changes in grain sizes and precipitates, resulting in a distinct microstructure from the base material, which affects the corrosion behaviour in different joint zones [5,6]. For dissimilar joints, in addition to the microstructure difference, the chemical composition inhomogeneity increases the difficulty of corrosion research.

In challenging environments featuring high humidity and elevated temperatures, aluminum joints are susceptible to corrosion, particularly when dissimilar materials are welded together and left unprotected [7]. Welds of dissimilar materials often exhibit pronounced heterogeneities, which can result in macro- and micro-galvanic corrosion [8].

For instance, CHEN et al [9] reported the changes in corrosion susceptibility of local regions, when corroding separated or combined areas within joints of 7050-T76 Al alloy. Consequently, galvanic-coupling corrosion between the zones can be catastrophic if both materials are conductive and exhibit considerably disparate corrosion potentials. Besides, many reports [10−12] indicate that the corrosion behaviour of joints is closely related to the microstructures and compositions. For instance, DONATUS and co-workers [10] considered that the HAZ at the side of AA6082 is the most susceptible region in the dissimilar friction stir welds (FSW) of AA5083-O and AA6082-T6 alloys. The concentration of Mg_2Si phases on the grain boundaries is the main reason. DENG et al [11−13] investigated the corrosion behaviour of high-strength aluminum alloys and their joints, and showed that galvanic corrosion could be formed due to the difference of microstructures. However, limited work has been done on the corrosion mechanism of dissimilar MIG joints of different series aluminum alloys, limiting their application.

In rail transportation, a large number of 5xxx series and 6xxx series Al alloys are used; therefore, it is inevitable to weld these two series alloys. Due to the difference in microstructures and chemical compositions, different series aluminum alloys have varying response to the effect of heat input during welding, which can be challenging for the corrosion research. The current study is motivated by the need to weld 6xxx and 5xxx alloys together for high-speed train applications. By exploring corrosion mechanisms, a wide range of corrosion data can be obtained for aluminum alloys, making them suitable for constructing parts and components in various fields of applications and enabling the possibility of combining and/or joining dissimilar aluminum alloy parts [7]. In this study, a new 6005A extrusion plate containing Sc and the 5083 rolling plate are selected for MIG welding, due to their promising applications in high-speed trains [2,14,15]. The relationship between the corrosion behavior of the dissimilar MIG joint and the microstructures of different zones is investigated.

2 Experimental

2.1 Materials and welding process

A new 6005A-T6 alloy extrusion plate containing Sc (designated as 6005A+Sc) and the 5083-H113 rolled plate were used in this study. The welding wire material is ER5087. Table 1 gives their chemical compositions. Two kinds of 8 mm-thick aluminum alloy plates were MIG welded on a Fronius TPS5000 welding machine. The welding direction was parallel to the rolling direction of the plates. Figure 1 illustrates the schematic diagram of the dissimilar joint, showing the sample dimensions used for various experiments.

Table 1 Chemical compositions of base alloys and welding wires (wt.%)

Material	Al	Mg	Si	Mn	Fe	Cu	Sc	Zr
6005A+Sc	Bal.	0.67	0.76	0.29	0.10	0.20	0.06	0.05
5083	Bal.	3.98	0.13	0.46	0.32	0.05	−	−
ER5087	Bal.	5.00	0.25	0.80	0.40	0.05	−	0.15

2.2 Microstructure characterization

A Lei Ka DM4M optical microscope was used to observe the microstructure of cross section of the dissimilar welded joint samples under polarized light. The samples were electrochemical polished and then were anodized in the Baker's solution (8 mL HBF_4 + 190 mL H_2O) at an electric potential of 20 V for 4.5 min.

The Sirion 200 field emission gun scanning electron microscope (SEM) equipped with energy dispersive X-ray spectroscopy (EDS) was used to identify the chemical element of coarse intermetallics in different microstructural zones. Detailed analyses of phase constituents were conducted using an X-ray diffractometer (Rigaku, SmartLab) with Cu $K_{\alpha 1}$ radiation (X-ray wavelength: 1.54 Å), scanning the range of approximately 20°−90°, employing a light tube voltage of 40 kV, a filament current of 30 mA, and a scanning rate of 1 (°)/min. The grain structures of different microstructural zones were further characterized by SEM with an electron backscattered diffraction (EBSD) detector. The samples of EBSD examination were ground, followed by mechanical and electrochemical polishing. In EBSD orientation maps, the red lines indicate the low angle grain boundaries (LAGBs) with misorientation angle between 2° and 15°, and the black lines indicate the high angle grain boundaries (HAGBs) with misorientation angle above 15°. Detailed data regarding grain structures were analyzed by using TSL OIM software.
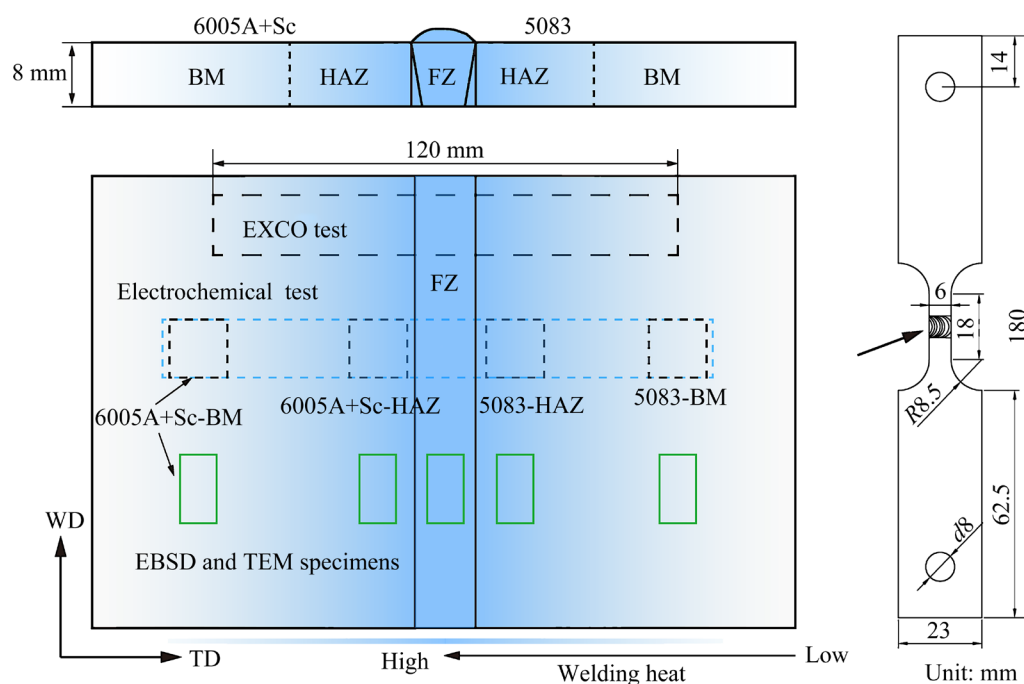
Fig. 1 Schematic diagram of welding joints used for microstructure observation and corrosion testing

To comprehensively investigate the grain microstructure and grain boundary precipitates (GBPs) across various zones, a FEI Tecnai G^2 F20 transmission electron microscope (TEM) equipped with a high angle annular dark-field (HAADF) detector and energy disperse spectroscopy (EDS) was used at an acceleration voltage of 200 kV. Thin foils for TEM observation were cut from different zones, followed by mechanical grinding to less than 80 μm and punching into 3 mm-thick disks. Subsequently, electropolishing was carried out by twin-jet electropolishing in an electrolyte solution consisting of 30 vol.% HNO_3 and 70 vol.% methanol at the temperature from −20 to −30 °C.

2.3 Slow-strain-rate test

To evaluate the stress corrosion cracking (SCC) susceptibility of the dissimilar welded joint, slow strain rate tests (SSRT) were carried out both in air and 3.5 wt.% NaCl solution, with a strain rate of $1 \times 10^{-6}\,s^{-1}$, according to GB 15970.7—2000. Rectangular tensile specimens with a gauge length of 18 mm and a width of 6 mm were used, as shown in Fig. 1. The long axis of specimens was perpendicular to welding direction. Subsequently, the fracture surfaces of the tested samples during SSRT in air and 3.5 wt.% NaCl solution were observed on a Sirion 200 field emission gun SEM,

operating at 20 kV.

2.4 Immersion corrosion test

For the intergranular corrosion (IGC) test, the upper surface of the dissimilar MIG joint was polished down to 1200 grit. Then, the sample was degreased using 10 wt.% NaOH, pickled with 30 vol.% HNO_3 solution, rinsed using acetone and deionized water and finally dried in air. According to the GB/T 7998—2005, the IGC tests were conducted in a solution of 30 g NaCl + 10 mL HCl +1 L distilled water at (35±2) °C for 24 h.

Exfoliation corrosion behaviors of different microstructural zones in joints were evaluated using immersion tests at room temperature in standard exfoliation corrosion solution (GB/T 22639—2008). Exfoliation corrosion solution was prepared as follows: dissolving 234 g NaCl and 50 g KNO_3 in water, adding 6.3 mL HNO_3 (70 wt.%), and diluting to 1 L. The solution consists of 4.0 mol/L NaCl, 0.5 mol/L KNO_3 and 0.1 mol/L HNO_3, with a pH of 0.4. After immersion tests, the corroded surface morphologies of different zones of the dissimilar MIG joint were observed on a Sirion 200 field emission gun SEM, operating at 20 kV.

The samples used for electrochemical tests were cut from different microstructural zones of the MIG joints. Then, the specimens were spot-welded

with copper lines on the back and cold mounted in epoxy. The area of the exposed surface of the specimens was 100 mm^2. The electrochemical measurements were performed using an electrochemical work station (MUL AUTO L5). The three-electrode electrochemical cell with a reference electrode of the saturated calomel electrode (SCE), an auxiliary electrode of the platinum sheet, and a working electrode of the specimen was used. The specimens for electrochemical experiments were immersed in 3.5 wt.% NaCl solution. To achieve a stable state in the electrode system, a 15 min open circuit potential (OCP) was applied to the samples. Then, electrochemical impedance spectroscopy (EIS) tests were carried out at an open circuit potential in the frequency ranging from 0.1 Hz to 100 kHz, using a 5 mV AC signal. The data were fit using ZView software. Finally, the potentiodynamic polarization tests were conducted, in which the applied potential ranged from −1.2 to −0.2 V with a scan rate of 5 mV/s. The corrosion potential (φ_{corr}) and the corrosion current density (J_{corr}) were determined by using the Tafel's extrapolation method.

3 Results

3.1 Slow-strain-rate tensile properties

Figure 2 shows the engineering stress vs engineering strain curves of the dissimilar MIG joints tested in air and 3.5 wt.% NaCl solution. All the tests were conducted at a slow strain rate of 1×10^{-6} s^{-1}, which is considered as an appropriate rate to induce measurable SCC for the Al alloy [16]. It is observed that with the strain increasing, the stress increases rapidly and then gradually reaches the peak value until failure. Both specimens exhibit similar stress−strain responses, regardless of the test environments, in air or NaCl solution. This may be attributed to the fact that Al−Mg−Si alloys possess a better resistance to stress corrosion cracking [14]. In order to visually quantify the stress corrosion cracking susceptibility of the dissimilar joints, Table 2 summarizes ultimate tensile strength (UTS),

elongation to failure (E_f), fracture time (T_f) and their corresponding indexes of susceptibility to SCC, P_{SCC}, which are calculated according to the following equation [17]:

$$P_{scc} = \frac{P_{NaCl}}{P_{Air}} \times 100\% \tag{1}$$

where P_{Air} and P_{NaCl} represent the property values measured in air and corrosive solution, respectively. P_{SCC} means the SCC susceptibility evaluated by three different property parameters: ultimate tensile strength (UTS), elongation to failure (E_f) and fracture time (T_f). The higher the P_{SCC} value is, the higher the SCC resistance is.

According to Table 2, UTS$_{SCC}$ reaches 102%, while $E_{f,SCC}$ and $T_{f,SCC}$ are 91.5% and 91.9%, respectively. This indicates that if the dissimilar joint is evaluated by strength factors, no obvious stress corrosion sensitivity is revealed. If it is evaluated by E_f and T_f, it shows a certain stress corrosion sensitivity. Figures 3(a, e) show macroscopic images of the dissimilar joints fractured in air and 3.5 wt.% NaCl solution, respectively. Two joints both fracture at 6005A+Sc-HAZ, indicating that this position is the weakest zone of the entire joint. The microscopic morphology of the fracture location was analyzed. In air, the fracture mode is ductile transgranular fracture. EDS results reveal small impurity particles containing Fe, Si and Mn,
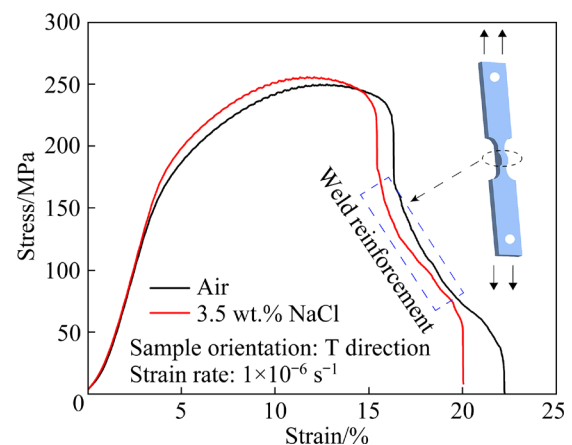

Fig. 2 Engineering stress vs engineering strain curves of dissimilar MIG joint failed in SSRT

Table 2 SSRT results and P_{scc} values

Corrosive environment	UTS/MPa	UTS$_{SCC}$/%	E_f/%	$E_{f,SCC}$/%	T_f/s	$T_{f,SCC}$/%
Air	250±2		22.4±0.8		223952	
3.5 wt.% NaCl	255±3	102.0	20.5±1.0	91.5	205891	91.9

as arrowed in Fig. 3(d). This implies that the formation, growth and coalescence of dimples are caused by breaking or debonding of impurity particles, like AlFeMnSi [18]. When the joint is exposed to corrosive environment, the fracture mode still remains as ductile transgranular fracture. Besides, ther is no obvious difference in the dimple size between the samples failed in air and 3.5 wt.% NaCl solution. Therefore, it can be concluded that the 6005A+Sc/5083 dissimilar joint exhibits excellent stress corrosion cracking resistance.

3.2 Intergranular corrosion performance

Figure 4 shows the cross section micrograph of the dissimilar joint after immersion in IGC solution for 24 h. Evidently, different microstructural zones show different IGC sensitivity. 6005A+Sc-BM exhibits severe IGC susceptibility with a corrosion depth of 41 μm (Fig. 4(a)), and its grain boundary is the preferentially corroded position. 6005A+ Sc-HAZ and FZ demonstrate high corrosion resistance, with a maximum corrosion depth of 10 μm and <10 μm, respectively. On the 6005A+Sc
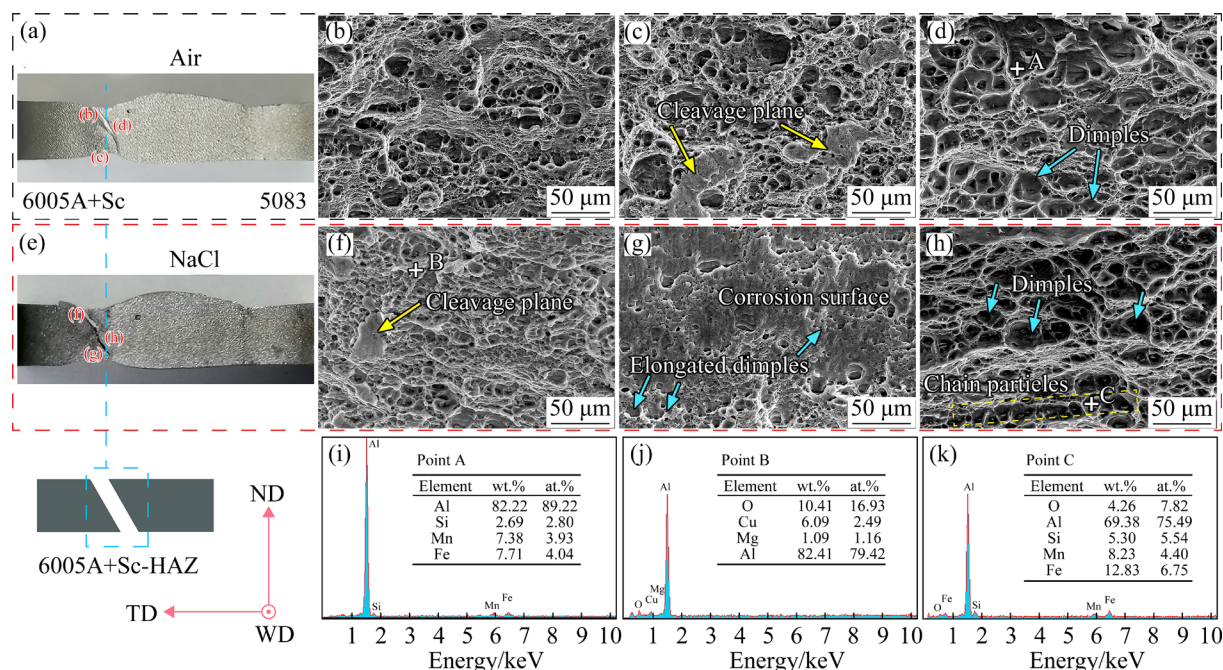

Fig. 3 SEM morphologies of tensile fracture of dissimilar joints after SSRT test in different corrosive environments: (a−d) In air; (e−h) In 3.5 wt.% NaCl solution; (i−g) EDS results
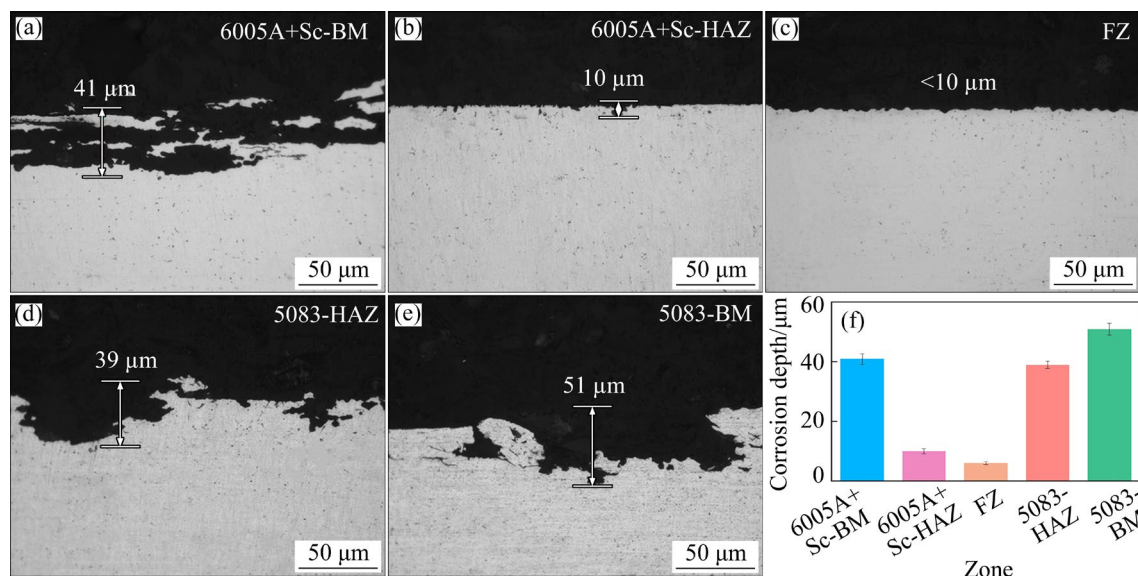

Fig. 4 Morphologies of IGC cross sections in different zones of dissimilar joint: (a) 6005A+Sc-BM; (b) 6005A+Sc-HAZ; (c) FZ; (d) 5083-HAZ; (e) 5083-BM; (f) Corrosion depth in different zones

side, the maximum corrosion depth values of heat-affected zone (HAZ) and base metal (BM) are 39 and 51 μm, respectively, showing higher IGC susceptibility.

The SEM surface images of the dissimilar joint after the EXCO tests are shown in Fig. 5. It is obvious that different microstructural zones exhibit different corrosion degrees. In the 6005A+Sc-BM, a large number of corrosion products flake off the matrix and EDS analyses reveal that their main compositions are Al, Cl and O elements. The exfoliation of corrosion products is attributed to wedge-shaped stresses generated by an increased volume of corrosion products at the grain boundaries, which lifts the surface grains [19]. In the 6005A+Sc-HAZ, the amount of corrosion products decreases noticeably, and no obvious corrosion products accumulate on the surface of FZ.

In the whole joint, the most seriously corrosion area is 5083-BM, where the corrosion products cover the entire surface. In the 5083-HAZ, no obvious corrosion products are observed and only a considerable number of corrosion pits are distributed along grain boundaries. In conclusion, the corrosion degree of different microstructrual zones is as follows: FZ < 6005A+Sc-HAZ < 5083-HAZ < 6005A+Sc-BM < 5083-BM.

3.3 Electrochemical corrosion performance

Figure 6(a) displays the representative OCP curves of different microstructural zones of joints. The OCP values were measured by immersing the samples in 3.5 wt.% NaCl solution for 15 min. It can be observed that the OCP values of different zones stabilize gradually as the immersion time increases. The FZ exhibits a more positive OCP value compared to other zones. Two BMs display more negative OCP values compared to two HAZs. Additionally, the potential difference between 5083-BM and FZ is significantly larger than that
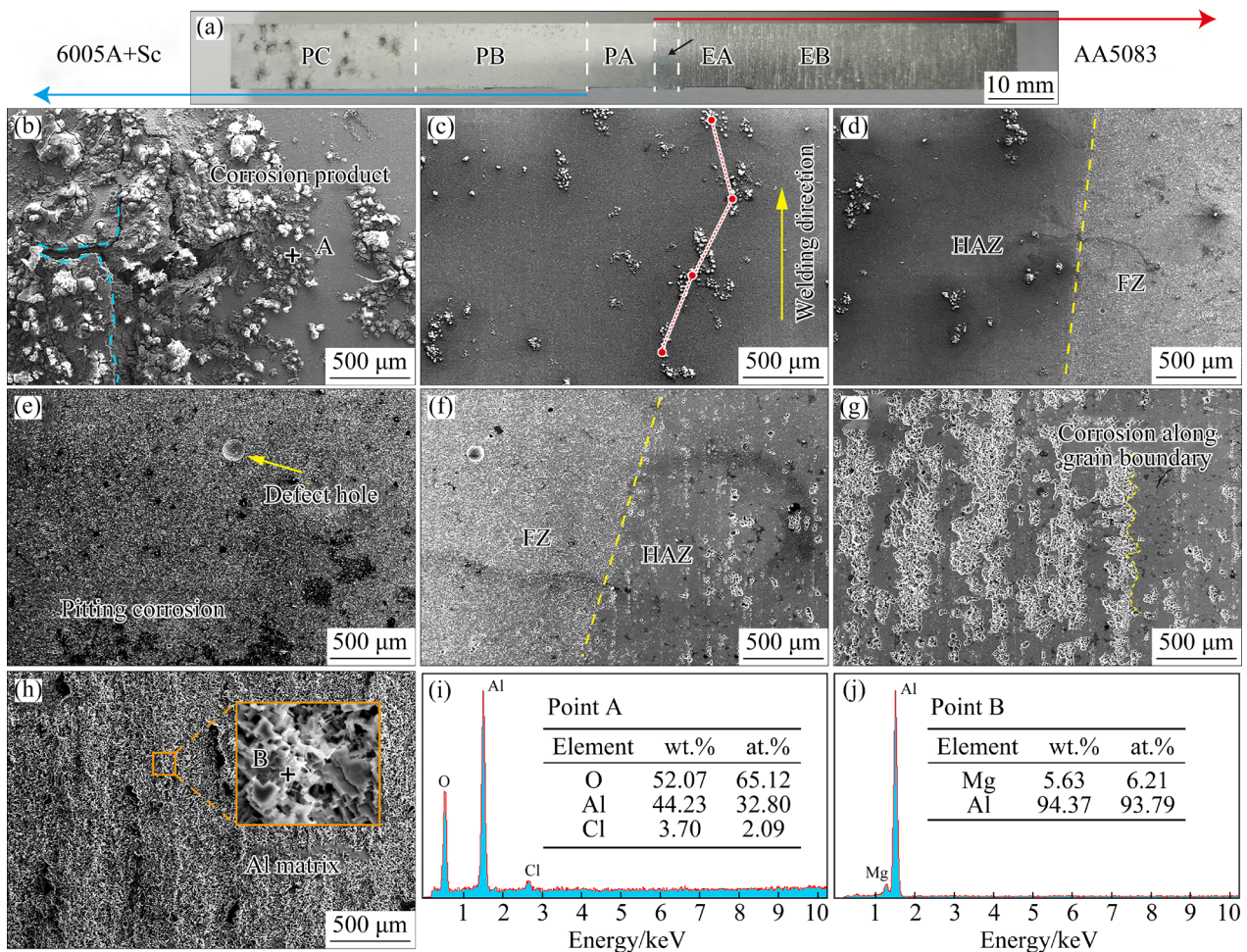

Fig. 5 SEM morphologies of dissimilar joint after EXCO tests: (a) Macroscopical image; (b) 6005A+Sc-BM; (c) 6005A+Sc-HAZ; (d) Transition zone between 6005A+Sc-HAZ and FZ; (e) FZ; (f) Transition zone between 5083-HAZ and FZ; (g) 5083-HAZ; (h) 5083-BM; (i, j) EDS results of selected points

between 6005A+Sc-BM and FZ. This potential difference between two different micro-zones can result in macroscopic galvanic coupling corrosion. The OCP value indicates the thermodynamic tendency of metallic materials to participate in the electrochemical corrosion reactions with the surrounding medium [20]. Based on these observations, it can be tentatively inferred that the FZ exhibits better corrosion resistance, and two HAZs are both less sensitive to corrosion than two BMs.

Figure 6(b) displays the polarization curves of different microstructural zones of the joint immersed in 3.5 wt.% NaCl solution. The variation trends of all polarization curves are similar, characterized by passivation (pitting). At the cathode branch, the current density remains almost constant with increasing potential, resulting in a low corrosion rate. As the potential approaches the self-corrosion potential, the polarization current density decreases to its minimum, causing the passivation film on the surface of the sample to break down, and the alloy becomes highly active. Relevant corrosion parameters are obtained via Tafel extrapolation and listed in Table 3. R_{corr} is the polarization resistance and can be calculated from

the following equation [21]:

$$R_{corr} = \left(\frac{\Delta\varphi}{\Delta J}\right)\varphi_{corr} = \left(\frac{1}{J_{corr}}\right)\frac{-\beta_c + \beta_a}{2.3(-\beta_c + \beta_a)} \quad (2)$$

where $\Delta\varphi$ and ΔJ are the polarization potential (V) and the polarization current density (mA/cm^2) respectively. φ_{corr} is the self-corrosion potential (V), J_{corr} is the current density (mA/cm^2), and β_a and β_c are the Tafel anode constant and cathode constant, respectively. The larger the R_{corr} value is, the higher the corrosion resistance is. Table 3 shows that FZ possesses the highest φ_{corr}, the lowest J_{corr} and the largest R_{corr}. Therefore, this area has the lowest corrosion sensitivity. The R_{corr} of the 6005A+ Sc-HAZ is slightly higher than that of the 6005A+ Sc-BM, showing higher corrosion resistance. The 5083-BM has the most negative φ_{corr}, the largest J_{corr} and the lowest R_{corr}, and thus this area has the lowest corrosion resistance. Therefore, the corrosion resistance of different zones from high to low is: FZ > 6005A+Sc-HAZ > 5083-HAZ > 6005A+Sc-BM > 5083-BM. These results are consistent with the immersion corrosion results in Section 3.2.

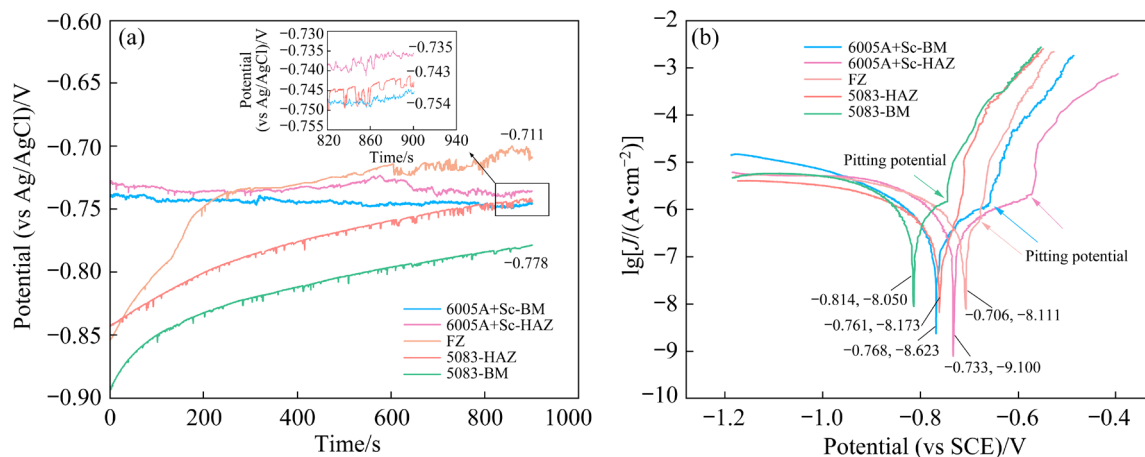Figure 7 shows the experimental and fitted Nyquist plots and Bode plots. Nyquist diagrams of

Fig. 6 Open circuit potential curves (a) and polarization curves (b) of different zones in dissimilar MIG joint

Table 3 Electrochemical parameters obtained from Tafel slope analyses in Fig. 6(b)

Zone	φ_{corr}(vs SCE)/V	$J_{corr}/(mA·cm^{-2})$	$-\beta_c/(V·dec^{-1})$	$\beta_a/(V·dec^{-1})$	$R_{corr}/(\Omega·cm^2)$
6005A+Sc-BM	−0.768	1.558±0.078	1.741	5.758	889.346
6005A+Sc-HAZ	−0.733	1.259±0.013	14.858	9.229	1965.978
FZ	−0.707	0.998±0.056	17.486	32.429	4949.195
5083-HAZ	−0.761	1.517±0.046	5.837	22.325	1344.133
5083-BM	−0.814	3.184±0.337	1.859	14.018	224.128

all specimens only consist of a single capacitive loop. This indicates that there is only charge transfer process, which may be linked to pitting and potentially passive dissolution [22]. Bode plot exhibits only a single time constant, as evidenced by the presence of only one maximum in the phase angle and no change in the slope in the Z modulus. According to literature [23], the variation in the angle of depression is directly associated with the change in the density of pitting, rather than the pitting depth. Furthermore, the reduction in the height and width of the maximum phase angle implies a decrease in the charge-transfer resistance. To quantitatively support our experimental findings and to better understand the metal's corrosion sensitivity, we used software Zview 2 to fit the electrochemical impedance spectrum to the equivalent circuit. The results are presented in Fig. 7(d) and Table 4. The physical significance of the elements of the equivalent circuit can be described as follows: R_s corresponds to the solution resistance and R_t is the charge transfer resistance. In our circuit, capacitance is mathematically modeled using a constant phase element (CPE) in order to obtain a better simulation results between the model and the experimental data. The impedance of a CPE can be calculated as

$$Z_{CPE} = \frac{1}{Y(jw)^n} \tag{3}$$

where Y is the admittance magnitude of the CPE constant, j is the imaginary unit, w is the angular frequency and n is the deviation parameter from 0 to 1. For $n=1$, 0 and 0.5, Z_{CPE} can be regarded as an ideal capacitance, a resistance and a Warburg impedance [24], respectively. Solution resistances (R_s) of different zones from the fitted results are listed in Table 4. R_t, as the primary polarization resistance (due to the surface passive layer), is directly linked to the corrosion rate. In comparison with R_t, R_s is found to be negligible. Moreover, the CPE-n value is observed to be 0.8−0.9 in all tested samples, which suggests a deviation from the ideal capacitive behavior ($n=1$). This represents the development of an inhomogeneous corroded surface, which may result from the dissolution of particles or the Al matrix [25]. Table 4 demonstrates that R_t value increases in the order of 5083-BM, 6005A+Sc-BM, 5083-HAZ, 6005A+Sc-HAZ and FZ. The larger the R_t value is, the slower the
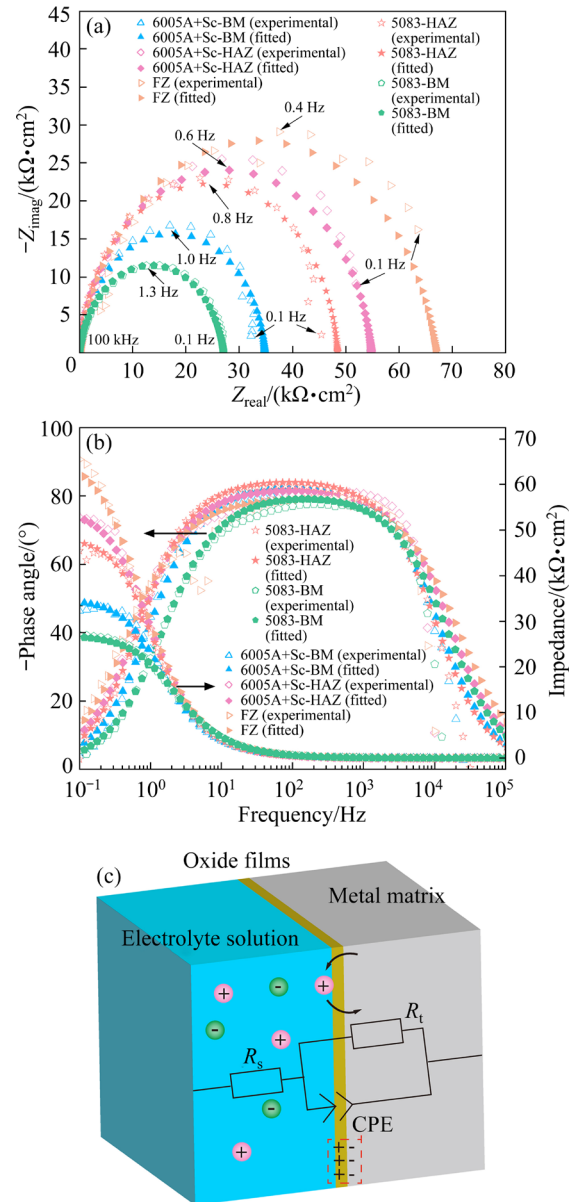

Fig. 7 Nyquist plots (a) and Bode plots (b) of different zones in dissimilar MIG joint, immersed in 3.5 wt.% NaCl solution, and equivalent circuit model proposed for fitting EIS data (c)

Table 4 Electrochemical parameters obtained by fitting analysis of impedance diagrams of different zones in dissimilar MIG joint immersed in 3.5 wt.% NaCl solution

Zone	R_s/ ($\Omega\cdot cm^2$)	R_t/ ($\Omega\cdot cm^2$)	CPE-T/ ($F\cdot cm^{-2}$)	CPE-n
6005A+Sc-BM	5.021	3.499×10^4	5.349×10^{-6}	0.93
6005A+Sc-HAZ	3.724	5.573×10^4	5.179×10^{-6}	0.91
FZ	5.085	6.754×10^4	5.383×10^{-6}	0.89
5083-HAZ	5.567	4.845×10^4	4.927×10^{-6}	0.95
5083-BM	6.696	2.703×10^4	5.005×10^{-6}	0.90

corrosion rate is. Thus, FZ has the highest corrosion resistance in the whole joint. EIS results further confirm that 5083-BM suffers the most severe corrosion during the test.

3.4 Microstructure

3.4.1 Grain boundary characteristics

Figures 8 and 9 show the EBSD orientation maps and misorientation angle distributions of different microstructural zones, respectively. The grains in the 6005A+Sc-BM (Fig. 8(a)) are elongated along the welding direction, showing typical pancake and fibrous bands, and the average grain size is about 6.71 μm with large length-to-width ratio. The 6005A+Sc-HAZ (Fig. 8(b)) is composed of subgrains with a grain size of about 5.79 μm, and its length-to-width ratio is smaller than that of the 6005A+Sc-BM. Figure 8(c) shows

Fig. 8 IPF of different zones in dissimilar MIG joint: (a) 6005A+Sc-BM; (b) 6005A+Sc-HAZ; (c) FZ; (d) 5083-HAZ; (e) 5083-BM (red: [001]; blue: [111]; green: [101])
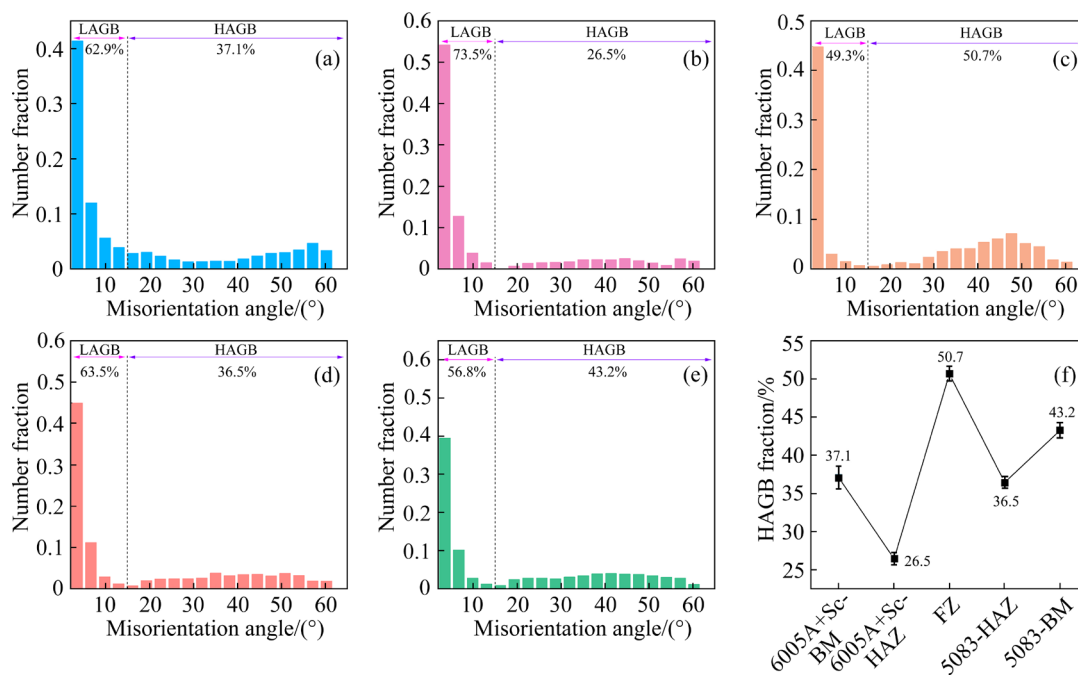

Fig. 9 Misorientation angle distribution of different zones in dissimilar MIG joint: (a) 6005A+Sc-BM; (b) 6005A+Sc-HAZ; (c) FZ; (d) 5083-HAZ; (e) 5083-BM; (f) HAGB fraction of different zones

that complete recrystallization occurs in the FZ. The diameter of the equiaxed grains is about 17.38 μm. At the 5083 side, as shown in Figs. 8(d, e), the grain sizes of the HAZ and the BM are 13.15 and 14.29 μm, respectively. The average grain sizes at the 5083 side are higher than those at 6005A+Sc side. Figure 9 shows the misorientation angle distributions of different zones. Compared with the BM, the HAGB fraction of the HAZ is lower. The HAGB fractions of the 6005A+Sc-BM, the 6005A+Sc-HAZ, the 5083-BM and the 5083-HAZ are 37.1%, 26.5%, 43.3%, and 36.5%, respectively. In the whole joint, the 5083-BM has the largest HAGB fraction and the largest grain size, and the most severe immersion corrosion. Therefore, grain size and HAGB are closely related to corrosion resistance.

3.4.2 Second phase distribution

The compositions of second phases determine their behaviour during corrosion tests [26,27]. Therefore, it is necessary to study the characteristics of second phases. Figure 10 shows XRD patterns of welding joints. At the 6005A+Sc side, Mg_2Si and AlFeMnSi are the main second phases. At the 5083 side, the primary second phases consist of Al_2Mg_3 and $Al_6(Mn,Fe)$, which is consistent with the results reported by SIMAR et al [28] and YASAKAU et al [29]. Figure 11 shows the distributions of the second phases. At the 6005A+Sc side, AlFeMnSi phase is fine and is distributed uniformly in the HAZ and BM. Mn is the primary alloying element in Al−Mg alloys, and most of it exists in the form of Al_6Mn phase. Additionally, the unavoidable Fe within the alloy undergoes eutectic reaction with Al
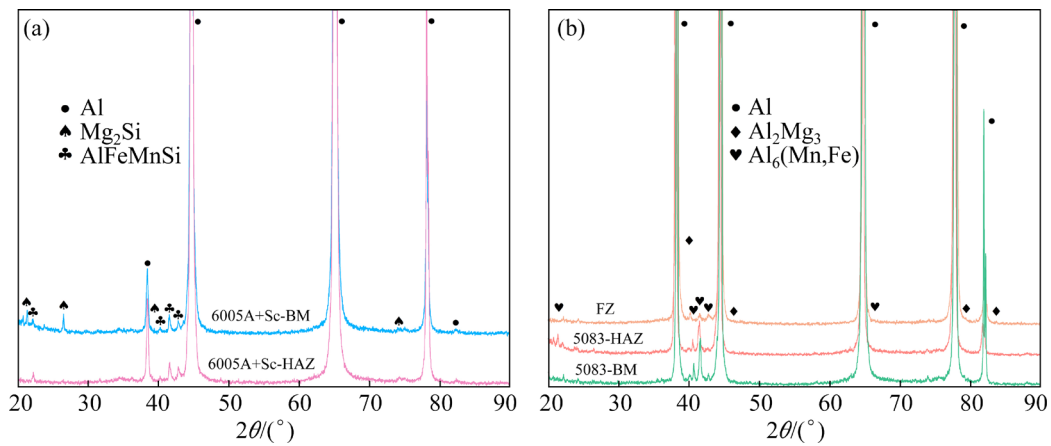

Fig. 10 XRD patterns of different zones in dissimilar MIG joint: (a) 6005A+Sc side; (b) FZ and 5083 side
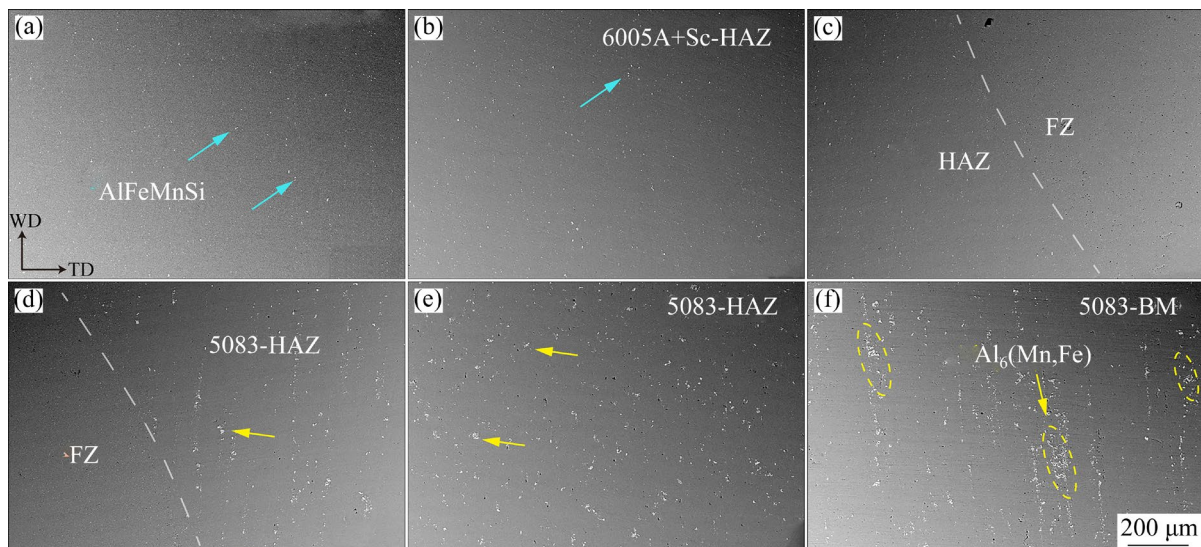

Fig. 11 Second phases distribution of different zones in dissimilar MIG joint in WD−TD plane: (a) 6005A+Sc-BM; (b) 6005A+Sc-HAZ; (c) 6005A+Sc-HAZ/FZ; (d) FZ/5083-HAZ; (e) 5083-HAZ; (f) 5083-BM

to form FeAl$_3$; this ultimately transforms Al$_6$Mn into more stable second-phase Al$_6$(Mn,Fe) in 5083 alloy [30]. The distributions of the Al$_6$(Mn,Fe) particles at the 5083 side are illustrated in Figs. 11(d−f). It can be found that compared with AlFeMnSi phase, Al$_6$(Mn,Fe) phase is coarse and distributed along the rolling direction (welding direction)

Figure 12 displays precipitates characterized by TEM in different microstructural zones of the joint. The precipitation sequence of Al−Mg−Si alloy is: supersaturated solid solution → GP zone → β'' (needle) → β' (rod) → β (plate) [31]. The strengthening effect of aging precipitates is $\beta'' > \beta' > \beta$. For the 6005A+Sc-BM, a large number of needle-shaped β'' precipitates are distributed along the $\langle 100 \rangle_{Al}$ direction, as shown in Fig. 12(a). The inserted image in Fig. 12(a) shows the selected area diffraction (SAD) pattern of Al matrix and β'' phases, with faint diffractions identifiable to β' phase. Affected by the welding heat, the main aging precipitates in 6005A+Sc-HAZ are β' phase, as indicated by the SAD pattern in Fig. 12(b). Furthermore, TEM image also verifies that the β'' precipitates disappear, and the rod-shaped precipitates (80−200 nm in length) become

predominant in the matrix. No obvious ageing precipitates are observed in the FZ since the ER5087 filler wire is a non-heat treatable alloy, as demonstrated in Fig. 12(c).

At the 5083 side, the short rod-shaped phases in the BM are mainly Al$_2$Mg$_3$, consistent with the results from YAN and HODGE [32] in 5xxx aluminum alloys. The Al$_2$Mg$_3$ phase has more negative corrosion potential than the aluminum matrix. Therefore, Al$_2$Mg$_3$ phase can lead to anodic dissolution of surrounding aluminum matrix, and decrease the corrosion resistance. There are many dislocations accumulating near the grain boundaries in the 5083-BM. Affected by welding heat cycle, the amount of dislocations gradually decreases in the 5083-HAZ. However, due to the short duration of welding process, the grains do not have enough time to recover entirely, and only some dislocations are rearranged to form subgrains.

Figure 13 depicts the grain boundary precipitates of different zones. In 6005A+Sc-BM (Figs. 13(a, b)), β'' phases predominate in the grains, while β phases are distributed uniformly at the grain boundary with no apparent precipitation-free zone (PFZ). In the 6005A+Sc-HAZ (Fig. 13(c)), the grain boundary precipitates became coarser and
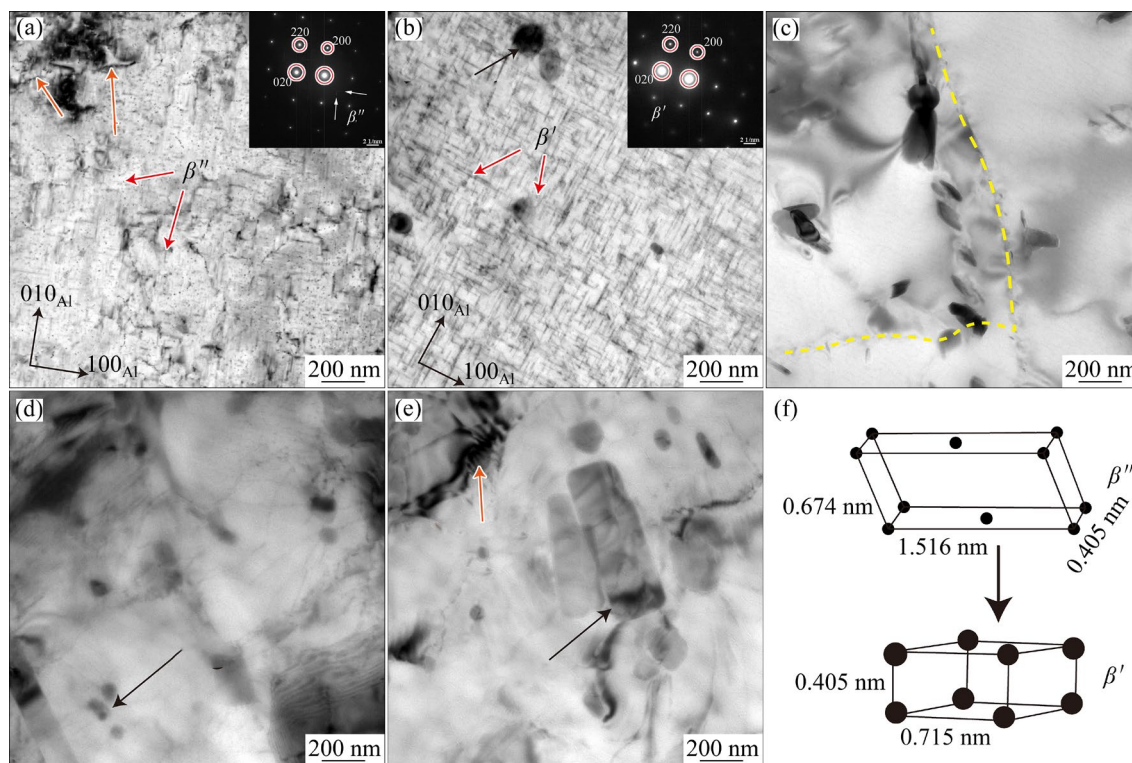

Fig. 12 TEM images of matrix precipitates of different zones: (a) 6005A+Sc-BM; (b) 6005A+Sc-HAZ; (c) FZ; (d) 5083-HAZ; (e) 5083-BM; (f) Schematic diagram of crystal structure of precipitates
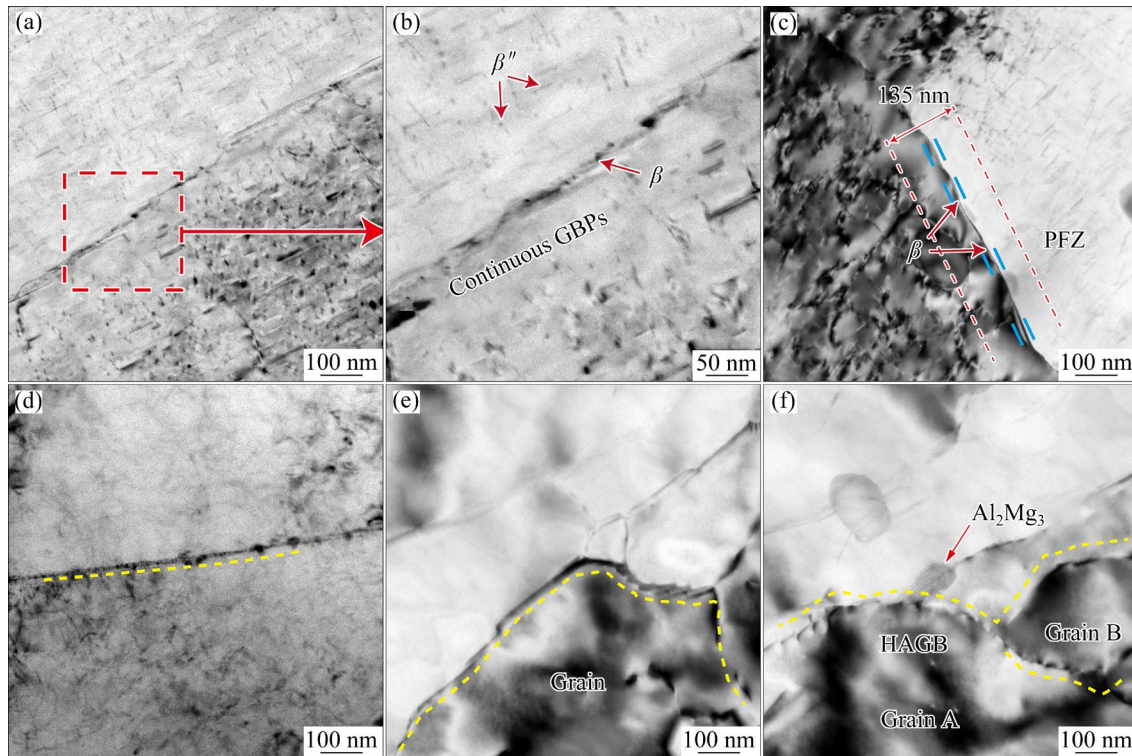
Fig. 13 TEM images of grain boundary precipitates in different zones: (a, b) 6005A+Sc-BM; (c) 6005A+Sc-HAZ; (d) FZ; (e) 5083-HAZ; (f) 5083-BM (GBPs−Grain boundary precipitates)

discontinuously distributed. The width of PFZ increases to 136 nm. At the 5083 side, as 5083 is a non-aging strengthened alloy, no obvious PFZ is observed in the HAZ and BM.

Grain boundary EDS mapping images of the BM and HAZ of 6005A+Sc alloys are presented in Fig. 14. Figure 14(a) indicates the presence of continuous and bright white phases located at the grain boundary of BM. The bright white phases are Mg_2Si, which can form anode corrosive channel, leading to a decrease in corrosion resistance [33]. Additionally, the white coarse and irregular phase is identified as AlFeMnSi, which has more positive corrosion potential than the Al matrix and β phase [34]. When exposed to corrosive conditions, AlFeMnSi can accelerate the dissolution of Al matrix and β phase. Figure 14(b) demonstrates that the grain boundary precipitates of HAZ are larger than those of BM, and become discontinuous.

4 Discussion

4.1 Stress corrosion mechanism

The microstructure and stress distribution are significantly affected by the thermal effects during welding, which can impact the joint's susceptibility to stress corrosion cracking [35]. In the current study, the dissimilar MIG joint exhibits a low stress corrosion sensitivity in 3.5 wt.% NaCl solution. During stress corrosion cracking [36], the surface passivation film is broken under stress-tension, exposing fresh metal to the corrosive environment, leading to the formation of a corrosion microcell between fresh metal and passivation film, as illustrated in Fig. 15. As Cl^- gradually accumulates on the metal surface, it undergoes a hydrolysis reaction, causing Al to lose electrons and become Al^{3+} while H^+ gains electrons to generate H_2 [37]. Therefore, corrosion current occurs in the aluminum base metal, but as the formed corrosion products cover the surface of the exposed area, H_2 cannot be diffused completely and ends up reacting with the confined area. Furthermore, electrochemical analysis reveals that an overall macroscopic corrosion cell exists between FZ and 6005A+Sc-HAZ, with the potentials of −0.71 and −0.75 V, respectively. This causes an accelerated corrosion rate in the 6005A+Sc-HAZ. However, as the applied stress increases, the larger PFZ width and weaker inter-granular bonding force in
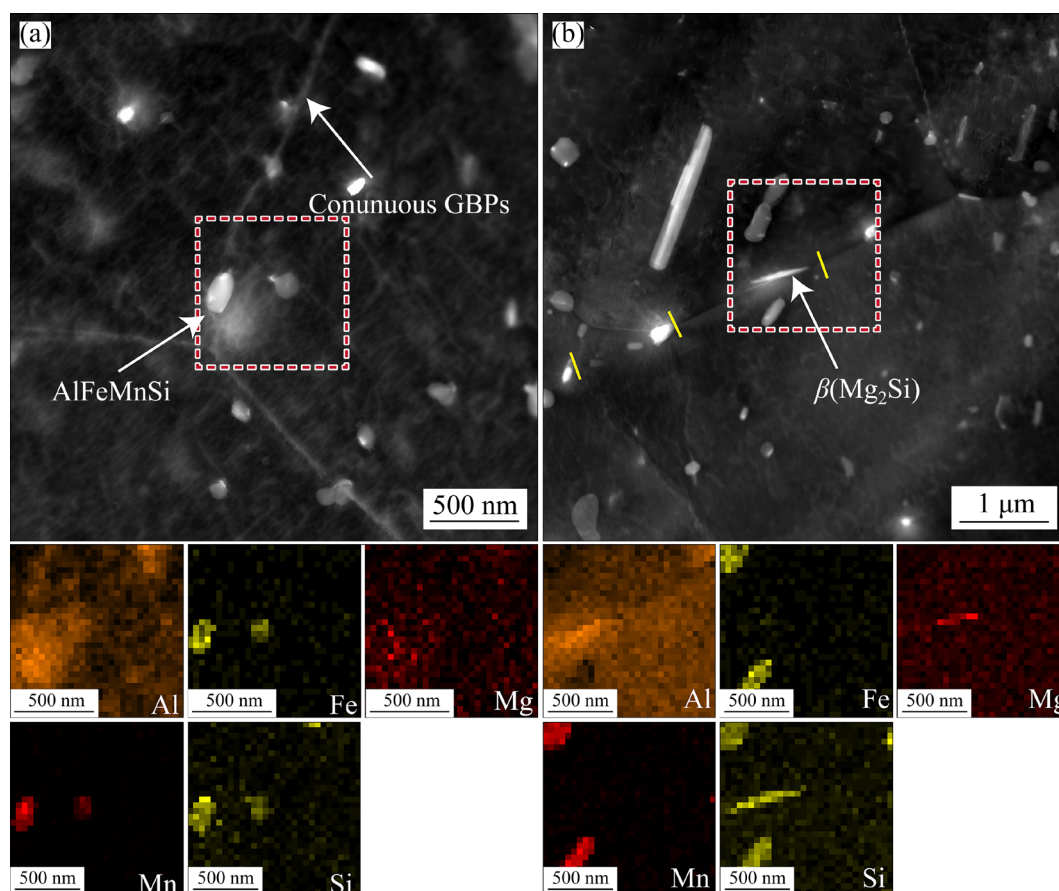
Fig. 14 Morphologies of grain boundary regions and corresponding EDS elemental mappings: (a) 6005A+Sc-BM; (b) 6005A+Sc-HAZ
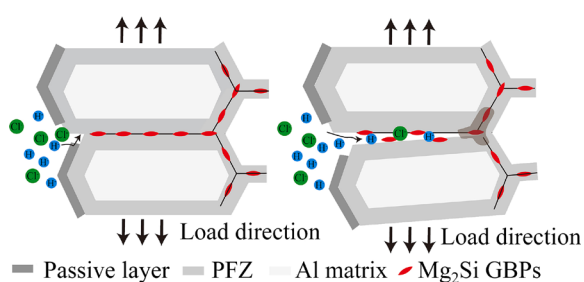

Fig. 15 Schematic diagram of fracture mechanism of dissimilar joint SSRT test in 6005A+Sc-HAZ

the 6005A+Sc-HAZ make the separation of grains easier, causing the residual hydrogen to diffuse along the grain boundaries and accelerate tension fracture.

4.2 Corrosion mechanism

The corrosion behaviour of different microstructural zones is closely related with their microstructures. Due to the small grain size and the re-dissolution of second phases, the FZ exhibits the best corrosion performance in the whole joint. As

for the 6005A+Sc-HAZ and 5083-HAZ, affected by welding heat [38], short-duration over-ageing and annealing treatments increase the proportion of sub-grain boundary and decrease the corrosion rate, which is consistent with the research work from SINHMAR and DWIVEDI [39]. In addition, from BM to HAZ, the aspect ratio of grains decreases and the exfoliation corrosion sensitivity decreases. This is because under the action of the wedge-shaped force of corrosion products, materials with a larger grain aspect ratio are more likely to reach the tearing conditions, exacerbating the degree of exfoliation corrosion [40]. However, it is important to note that corrosion is influenced by multiple factors such as matrix precipitates, grain boundary precipitates, and second phases. After welding and long-term natural aging, the main precipitates in the BM and HAZ of 6005A+Sc are β'' and β' [41], as shown in Fig. 12. Mg atoms in these precipitates are preferentially dissolved during the corrosion process, and grain boundary precipitates (β phases) have more negative anode potential with respect to

the Al matrix and PFZ, making them easier to dissolve in the cell [42], thereby accelerating the propagation rate of intergranular corrosion due to the continuous distribution of β (Mg$_2$Si) phases along the grains, as shown in Fig. 16.
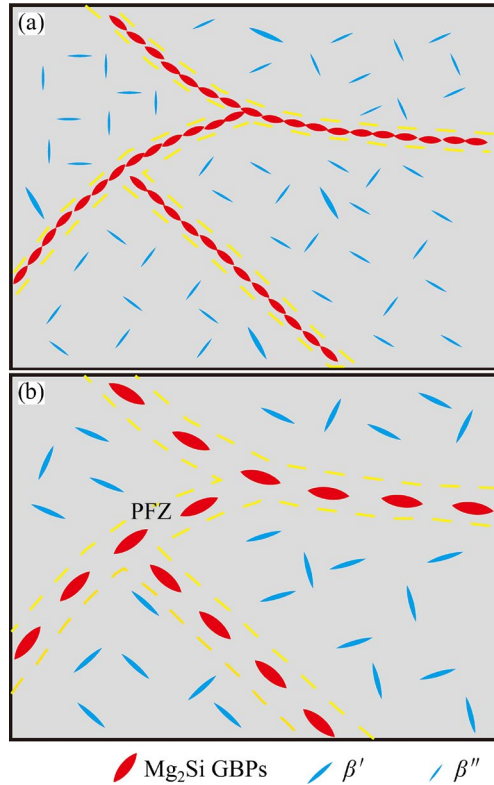

Fig. 16 Schematic diagram of microstructure in 6005A+Sc side of dissimilar joint: (a) 6005A+Sc-BM; (b) 6005A+Sc-HAZ

Figures 5(g, h) show that BM and HAZ at the 5083 side are sensitive to corrosion. This is because the corrosion potential of the Al$_2$Mg$_3$ phase is more negative than that of the Al matrix. As the anode phase, the Al$_2$Mg$_3$ is preferentially dissolved in the corrosive environment, thus reducing the corrosion resistance of the 5083 [43]. In addition, dislocations can be clearly observed in the 5083-BM grain boundaries, where the grains with higher stored-energy can accelerate the anodic dissolution. As shown in Fig. 5(g), there are obvious directional and uniformly distributed pitting corrosion at the 5083 side, which result from the preferential dissolution of Al matrix (anode) surrounding the Al$_6$(Mn,Fe) phases in the corrosive medium: Al→Al^{3+}+3e. Additionally, when the second phase acts as a cathode, it can generate OH$^-$ through the following reaction [44]: O$_2$+4H$_2$O+4e=4OH$^-$. With the prolongation of the corrosion time, the grooves

around the Al matrix dissolve completely, connecting with each other and resulting in the detachment of the second phases and ultimately forming severe corrosion. The corrosion schematic is illustrated in Fig. 17. Compared with the 5083-BM, due to the dissolution of Al$_2$Mg$_3$ phase, the corrosion degree of 5083-HAZ is significantly reduced.
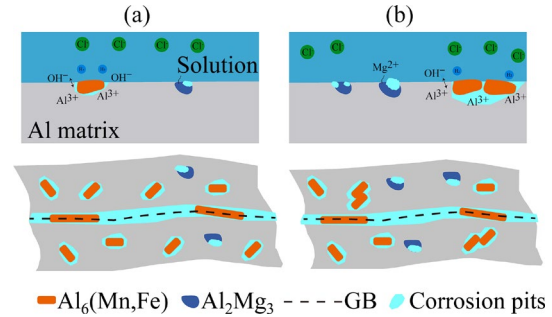

Fig. 17 Schematic diagram of corrosion at 5083 side for dissimilar joint: (a) 5083-HAZ; (b) 5083-BM

In a corrosive environment, the difference in corrosion potential among different microstructural zones leads to the formation of galvanic corrosion. Electrochemical results show that the corrosion potential of the BM is more negative than that of the FZ and HAZ. This indicates that BM acts as an anode and the HAZ and the FZ serve as cathodes. The HAZ and FZ, which have lower mechanical properties, act as cathodes in the sacrificial anode method [45], leading to an improvement in regional corrosion resistance and prolonging the service life of the dissimilar joint.

5 Conclusions

(1) The UTS$_{SCC}$, $E_{f,SCC}$ and $T_{f,SCC}$ of 6005A+Sc/5083 dissimilar joint are 102%, 91.5% and 91.9%, respectively, and the joint fractures at 6005A+Sc-HAZ.

(2) The results from intergranular corrosion (IGC) test, exfoliation corrosion (EXCO) test and electrochemical corrosion test consistently demonstrate the same order of corrosion resistance: FZ > 6005A+Sc-HAZ > 5083-HAZ > 6005A+Sc-BM > 5083-BM.

(3) The low corrosion resistance of 5083-BM and 5083-HAZ can be attributed to the presence of numerous Al$_2$Mg$_3$ phases and micro-scaled Al$_6$(Mn,Fe) intermetallics.

(4) The high corrosion resistance of 6005A+ Sc-BM and 6005A+Sc-HAZ can be attributed to the discontinuously distributed grain boundary precipitates (β-Mg$_2$Si), the smaller grain size, and the lower corrosive current density.

CRediT authorship contribution statement

Guo-fu XU: Supervision; **Liang LIU:** Experiment, Writing − Original draft; **Ying DENG:** Methodology, Supervision, Project administration, Writing − Review & editing; **Yu ZENG:** Investigation; **Jun-chang CAO:** Experiment; **Lei TANG:** Investigation; **Xiao-yan PENG:** Investigation; **Jia-qi DUAN:** Methodology, Writing – Editing; **Mei-chan LIANG:** Investigation; **Qing-lin PA:** Supervision.

Declaration of competing interest

The authors declare that they have no known competing financial interests or personal relationships that could have appeared to influence the work reported in this paper.

Acknowledgments

References

[1] LIU Liang, XU Guo-fu, DENG Ying, YU Qing-bin, LI Guo-liang, ZHANG Li-gang, LIU Bing, FU Le, PAN Qing-lin. Existing form of Sc in metal-inert gas welded Al−0.60Mg−0.75Si alloy and its role in welding strength [J]. Materials Characterization, 2023, 197: 112649.

[2] ZHU Xin-wen, DENG Ying, LAI Yi, GUO Yi-fan, YANG Zi-ang, FU Le, XU Guo-fu, HUANG Ji-wu. Effects of Al$_3$(Sc$_{1−x}$Zr$_x$) nano-particles on microstructure and mechanical property of friction-stir-welded Al−Mg−Mn alloys [J]. Transactions of Nonferrous Metals Society of China, 2023, 33: 25−35.

[3] MAGGIOLINO S, SCHMID C. Corrosion resistance in FSW and in MIG welding techniques of AA6xxx [J]. Journal of Materials Processing Technology, 2008, 197: 237−240.

[4] DENG Cheng-min, WANG Cai-mei, WANG Fei-fan, SONG Bao-yong, ZHANG Hua. Effect of microstructure evolution on corrosion behavior of 2195 Al−Li alloy friction stir welding joint [J]. Materials Characterization, 2022, 184: 111652.

[5] SAKTHIVEL P, MANOBBALA V, MANIKANDAN T, MOHAMMED ARMAN SALIK Z, RAJKAMAL G. Investigation on mechanical properties of dissimilar metals using MIG welding [J]. Materials Today: Proceedings, 2021, 37: 531−536.

[6] IMAM FAUZI E R, CHE JAMIL M S, SAMAD Z, MUANGJUNBUREE P. Microstructure analysis and mechanical characteristics of tungsten inert gas and metal inert gas welded AA6082-t6 tubular joint: A comparative study [J]. Transactions of Nonferrous Metals Society of China, 2017, 27: 17−24.

[7] SQUILLACE A, DE FENZO A, GIORLEC G, BELLUCCI F. A comparison between FSW and TIG welding techniques: Modifications of microstructure and pitting corrosion resistance in AA 2024-T3 butt joints [J]. Journal of Materials Processing Technology, 2004, 152: 97−105.

[8] WON S, SEO B, PARK J M, KIM K H, SONG K H, MIN S H, HA T K, PARK K. Corrosion behaviors of friction welded dissimilar aluminum alloys [J]. Materials Characterization, 2018, 144: 652–660.

[9] CHEN Yong, WANG Yan-qiu, ZHOU Li, MENG Guo-zhe, LIU Bin, WANG Jun-ji, SHAO Ya-wei, JIANG Jian-tang. Macro-galvanic effect and its influence on corrosion behaviors of friction stir welding joint of 7050-T76 Al alloy [J]. Corrosion Science, 2020, 164: 108360.

[10] DONATUS U, THOMPSON G E, ZHOU X, WANG J, CASELL A, BEAMISH K. Corrosion susceptibility of dissimilar friction stir welds of AA5083 and AA6082 alloys [J]. Materials Characterization, 2015, 107: 85–97.

[11] DENG Ying, YE Rui, XU Guo-fu, YANG Ji-dong, PAN Qing-lin, PENG Bing, CAO Xiao-wu, DUAN Yu-lu, WANG Ying-jun, LU Li-ying, YIN Zhi-min. Corrosion behaviour and mechanism of new aerospace Al−Zn−Mg alloy friction stir welded joints and the effects of secondary Al$_3$Sc$_x$Zr$_{1−x}$ nanoparticles [J]. Corrosion Science, 2015, 90: 359−374.

[12] DENG Ying, YIN Zhi-min, ZHAO Kai, DUAN Jia-qi, HU Jian, HE Zhen-bo. Effects of Sc and Zr microalloying additions and aging time at 120 °C on the corrosion behaviour of an Al−Zn−Mg alloy [J]. Corrosion Science, 2012, 65: 288−298.

[13] DENG Ying, YANG Zi-ang, ZHANG Guo. Nanostructure characteristics of Al$_3$Sc$_{1−x}$Zr$_x$ nanoparticles and their effects on mechanical property and SCC behavior of Al−Zn−Mg Alloys [J]. Materials, 2020, 13: 1909.

[14] MA Ji-jun, SUN Jing, GUAN Quan-mei, YANG Qing-wei, TANG Jian, ZOU Cheng-xiong, WANG Jun, TANG Bin, KOU Hong-chao, WANG Hai-sheng, GAO Jun, LI Jin-shan, WANG W Y. The localized corrosion and stress corrosion cracking of a 6005A-T6 extrusion profile [J]. Materials, 2021, 14: 4924.

[15] PENG Yong-yi, LI Shu, DENG Ying, ZHOU Hua, XU Guo-fu, YIN Zhi-min. Synergetic effects of Sc and Zr microalloying and heat treatment on mechanical properties and exfoliation corrosion behavior of Al−Mg−Mn alloy [J]. Materials Science and Engineering A, 2016, 66: 61−71.

[16] JONES R H, VETRANO J S, WINDISCH C F. Stress corrosion cracking of Al−Mg and Mg−Al alloys [J]. Corrosion, 2004, 60: 1144−1154.

[17] DENG Ying, PENG Bing, XU Guo-fu, Pan Qing-lin, YE Rui, WANG Ying-jun, LU Li-ying, YIN Zhi-min. Stress corrosion cracking of a high-strength friction-stir-welded joint of an Al−Zn−Mg−Zr alloy containing 0.25 wt.% Sc [J]. Corrosion Science, 2015, 100: 57−72.

[18] CHEN Xia-ming, WANG Xiao-nan, DONG Qi-peng, YU Jia-min, ZHU Zhen, NAGAUMI H. The effect of AlFeSi intermetallics compounds morphology on the corrosion behavior of Al−Mg−Si alloy laser welds [J]. Journal of Materials Research and Technology, 2021, 14: 1203−1207.

[19] MARLAUD T, MALKI B, HENON C, DESCHAMPS A, BAROUX B. Relationship between alloy composition, microstructure and exfoliation corrosion in Al−Zn−Mg−Cu alloys [J]. Corrosion Science, 2011, 53: 3139−3149.

[20] WEI Bo, PAN Shuai, LIAO Gui-zhen, ALI A, WANG Shuang-bao. Sc-containing hierarchical phase structures to improve the mechanical and corrosion resistant properties of Al−Mg−Si alloy [J]. Materials & Design, 2022, 218: 110699.

[21] JIANG Fu-qing, HUANG Ji-wu, JIANG Ying-ge, XU Cheng-long. Effects of quenching rate and over-aging on microstructures, mechanical properties and corrosion resistance of an Al–Zn–Mg (7046A) alloy [J]. Journal of Alloys and Compounds, 2021, 854: 157272.

[22] DAVOODI A, ESFAHANI Z, SARVGHAD M. Microstructure and corrosion characterization of the interfacial region in dissimilar friction stir welded AA5083 to AA7023 [J]. Corrosion Science, 2016, 107: 133−144.

[23] MCMAHON M E, SCULLY J R, BURNS J T. Mitigation of intergranular stress corrosion cracking in Al−Mg by electro-chemical potential control [J]. JOM, 2017, 69: 1389−1397.

[24] ASSIS S L, WOLYNEC S, COSTA I. Corrosion characterization of titanium alloys by electrochemical techniques [J]. Electrochimica Acta, 2006, 51: 1815−1819.

[25] BEURA V K, KALE C, SRINIVASAN S, WILLIAMS C L, SOLANKI K N. Corrosion behavior of a dynamically deformed Al−Mg alloy [J]. Electrochimica Acta, 2020, 354: 136695.

[26] ANDREATTA F, TERRYN H, DE WIT J H W. Effect of solution heat treatment on galvanic coupling between intermetallics and matrix in AA7075-T6 [J]. Corrosion Science, 2003, 45: 1733−1746.

[27] CHEN Xia-ming, DONG Qi-peng, LIU Zhen-guang, WANG Xiao-nan, ZHANG Qing-yu, HU Zeng-rong, NAGAUMI H. Fe-bearing intermetallics transformation and its influence on the corrosion resistance of Al−Mg–Si alloy weld joints [J]. Journal of Materials Research and Technology, 2020, 9: 16116−16125.

[28] SIMAR A, BRECHET Y, DE MEESTER B, DENQUIN A, PARDOEN T. Microstructure, local and global mechanical properties of friction stir welds in aluminium alloy 6005A-T6 [J]. Materials Science and Engineering A, 2008, 486: 85−95.

[29] YASAKAU K A, ZHELUDKEVICH M L, LAMAKA S V, FERREIRA M G S. Role of intermetallic phases in localized corrosion of aa5083 [J]. Electrochimica Acta, 2007, 52: 7651−7659.

[30] RAGHAVAN A, KOO J Y, STEEDS J W, PARK B K. Microanalytical study of the heterogeneous phases in commercial Al−Zn−Mg−Cu alloys [J]. Metallurgical Transactions A, 1985, 16: 1925−1936.

[31] RAVI C. First-principles study of crystal structure and stability of Al−Mg−Si−(Cu) precipitates [J]. Acta Materialia, 2004, 52: 4213−4227.

[32] YAN Jian-feng, HODGE A M. Study of β precipitation and layer structure formation in Al 5083: The role of dispersoids and grain boundaries [J]. Journal of Alloys and Compounds, 2017, 703: 242−250.

[33] UEMATSU Y, TOKAJI K, TOZAKI Y, KURITA T, MURATA S. Effect of re-filling probe hole on tensile failure and fatigue behaviour of friction stir spot welded joints in Al−Mg−Si alloy [J]. International Journal of Fatigue, 2008, 30: 1956−1966.

[34] BRITO C, VIDA T, FREITAS E, CHEUNG N, SPINELLI J E, GARCIA A. Cellular/dendritic arrays and intermetallic phases affecting corrosion and mechanical resistances of an Al−Mg−Si alloy [J]. Journal of Alloys and Compounds, 2016, 673: 220−230.

[35] WENG Yao-yao, JIA Zhi-hong, DING Li-peng, LIAO Jin, ZHANG Ping-ping, XU Ya-qi, LIU Qing. Effect of pre-straining on structure and formation mechanism of precipitates in Al−Mg−Si−Cu alloy [J]. Transactions of Nonferrous Metals Society of China, 2022, 32: 436−447.

[36] YUAN Ding-ling, CHEN Song-yi, CHEN Kang-hua, HUANG Lan-ping, CHANG Jiang-yu, ZHOU Liang, DING Yun-feng. Correlations among stress corrosion cracking, grain-boundary microchemistry, and zn content in high Zn-containing Al−Zn−Mg−Cu alloys [J]. Transactions of Nonferrous Metals Society of China, 2021, 31: 2220−2231.

[37] PENG Can, LIU Yu-wei, GUO Ming-xiao, GU Tian-zhen, WANG Chuan, WANG Zhen-yao, SUN Cheng. Corrosion and pitting behavior of pure aluminum 1060 exposed to nansha islands tropical marine atmosphere [J]. Transactions of Nonferrous Metals Society of China, 2022, 32: 448−460.

[38] LIU Qian, FANG Lei-ming, XIONG Zheng-wei, YANG Jia, TAN Ye, LIU Yi, ZHANG You-jun, TAN Qing, HAO Chen-chun, CAO Lin-hong, LI Jun, GAO Zhi-peng. The response of dislocations, low angle grain boundaries and high angle grain boundaries at high strain rates [J]. Materials Science and Engineering A, 2021, 822: 141704.

[39] SINHMAR S, DWIVEDI D K. Effect of weld thermal cycle on metallurgical and corrosion behavior of friction stir weld joint of AA2014 aluminium alloy [J]. Journal of Manufacturing Processes, 2019, 37: 305−320.

[40] NAVASER M, ATAPOUR M. Effect of friction stir processing on pitting corrosion and intergranular attack of 7075 aluminum alloy [J]. Journal of Materials Science & Technology, 2017, 33: 155−165.

[41] ZOU Yun, LIU Qing, JIA Zhi-hong, XING Yuan, DING Li-peng, WANG Xue-li. The intergranular corrosion behavior of 6000-series alloys with different Mg/Si and Cu

content [J]. Applied Surface Science, 2017, 405: 489−496.

[42] LIU Xin-yi, ZHANG Di-yao, WANG Cheng-chong, WANG Xu, ZHAO Zi-jun, WU Ming, HUANG J C. Effect of grain boundary precipitation on corrosion of heating-aging treated Al−4.47Zn−2.13Mg−1.20Cu alloy [J]. Journal of Materials Research and Technology, 2020, 9: 5815−5826.

[43] QIN Jin, LI Zhi, MA Ming-yang, YI Dan-qing, WANG Bin. Diversity of intergranular corrosion and stress corrosion cracking for 5083 Al alloy with different grain sizes [J]. Transactions of Nonferrous Metals Society of China, 2022,

32: 765−777.

[44] JIN Jun-jun, LU Wei, FU Zheng-hong, ZHU Zhong-yin, CHEN Wen-jing, GOU Guo-qing. Corrosion fatigue crack growth in A7N01S−T5 aluminum alloy MIG welded joints [J]. Journal of Materials Research and Technology, 2023, 23: 2202−2218.

[45] ABOOTALEBI O, KERMANPUR A, SHISHESAZ M R, GOLOZER M A. Optimizing the electrode position in sacrificial anode cathodic protection systems using boundary element method [J]. Corrosion Science, 2010, 52: 678−687.

Sc 改性的 6005A 和 5083 铝合金惰性气体保护焊异种接头的显微组织特征和腐蚀行为

徐国富 [1,2]，刘 亮 [1]，邓 英 [1,2]，曾 渝 [3]，曹俊昌 [1]，唐 磊 [1]，彭小燕 [1]，段佳琦 [4]，梁美婵 [5]，潘清林 [1]

1. 中南大学 材料科学与工程学院，长沙 410083；
2. 中南大学 粉末冶金国家重点实验室，长沙 410083；
3. 宝山钢铁股份有限公司，上海 201900；
4. Warwick Manufacturing Group, The University of Warwick, Coventry, CV4 7AL, UK;
5. 广东伟业铝厂集团有限公司，佛山 528000

摘　要：采用腐蚀测试和电子显微组织表征方法，研究了 Sc 改性的 6005A(6005A+Sc)和 5083 铝合金惰性气体保护焊异种接头的显微组织特征和腐蚀行为。结果表明：异种接头具有高应力腐蚀抗力，经慢应变速率拉伸测试后仍保留高强度。6005A+Sc 侧热影响区和基材区的抗晶间腐蚀和剥落腐蚀性能均高于 5083 侧相应区，这主要是因为 5083 侧的基材区和热影响区沿轧制方向存在大量的 Al_2Mg_3 相和微米级别的 $Al_6(Mn,Fe)$ 晶间相；而 6005A+Sc 侧基材区和热影响区 β-Mg_2Si 相非连续分布在晶界，且具有较小晶粒尺寸和低的腐蚀电流密度。

关键词：惰性气体保护焊；异种接头；铝合金；腐蚀；显微组织

(Edited by Bing YANG)